EARTH OBSERVATION AND GEOMATICS ENGINEERING

website: https://eoge.ut.ac.ir

Improved Cross-Range Resolution 2D Ground-Based SAR to Monitor Remote Objects

Benyamin Hosseiny [1], Jalal Amini [1*], Negar Zahedi [1]

[1] School of Surveying and Geospatial Engineering, College of Engineering, University of Tehran, Tehran, Iran

Article history:

Received: 2022-02-24, Received in revised form: 2022-3-16, Accepted: 2022-4-09

ABSTRACT

This study demonstrates the effectiveness of the combination of two-dimensional mechanical rail with mmWave multiple-input multiple-output (MIMO) radar in order to improve the target detection resolution and increase the quality of the obtained synthetic aperture radar (SAR) image. Ground-based SAR (GBSAR) systems cover a wide range of applications in remote sensing. In the past few years, mmWave MIMO radars have shown interesting potential in this field due to their low cost, compact size, and high phase sensitivity. MIMO capability enables the angular discrimination of multiple targets in the same range as the radar sensor. However, current mmWave MIMO radars do not provide a high angular resolution that suffices in earth observation applications. To this end, we demonstrate the feasibility of combining mechanical rail and MIMO radars to obtain better cross-range resolution. Our experiments show that the ground-based MIMO SAR can obtain about 20 times better cross-range resolution than MIMO radar while improving the image quality with more than 10 dB improvement in the peak sidelobe ratio (PSLR) and signal to clutter ratio (SCR). Moreover, we provide a deeper investigation and comparison between the MIMO GBSAR and conventional monostatic GBSAR images. According to the results, MIMO GBSAR provided a similar angular resolution and PSLR but with a lower SCR than the monostatic GBSAR. The effects of mechanical rail instability are also investigated. According to the obtained results, the rail's instability causes around a 5 dB decrease in the obtained SAR image's focusing capability.

KEYWORDS

mmWave,
Multiple-Input Multiple-Output (MIMO),
Radar,
GBSAR,
Geo-Radar,
Terrestrial Radar

1. Introduction

Remote sensing is one of the powerful and advanced tools for observing and measuring natural hazards such as rockslides (Tarchi et al., 2005), landslides (Luzi et al., 2006), volcanoes (Intrieri et al., 2013), avalanches (Martinez-Vazquez & Fortuny-Guasch, 2008), ice movement (Luzi et al., 2007), and also monitor man-made artificial artifacts such as displacements caused by the construction of dams (Luzi et al., 2010), tall buildings (Artese & Nico, 2020) or bridges (Miccinesi et al., 2021) and open-pit mines (Farina, 2011). It also identifies moving objects to monitor sea traffic

* Corresponding Author
E-mail addresses: jamini@ut.ac.ir (J. Amini)

(Ao & Datcu, 2018) and urban traffic (Weihing et al., 2006).

In recent years, due to the daily progress of technologies, remote sensing society has also made huge developments, such as a wide range of large-scale space platforms to small-scale ground-based platforms for monitoring the earth's surface. Remote sensors are used in different electromagnetic spectrum wavelengths, from visible light to radar waves. Radar, as an active sensor, can produce the transmitted waves itself; thus, it has the possibility of acquiring data during the day and night. Moreover, radar's long wavelength (compared to the visible and infrared wavelengths) is insensitive to weather conditions (Bamler & Hartl, 1998; Ulaby et al., 2014).

Radar can typically detect and discriminate targets along its line of sight, while it cannot discriminate targets located in the same range bin but with different angles with respect to the radar (Richards et al., 2010). Synthetic Aperture Radar (SAR) is a radar imaging technique that enables radar cross-range discriminability as well as the range direction. Accordingly, resolution along the range and cross-range in these systems depends on the operating signal's frequency bandwidth and the physical length of the radar antenna, respectively (Carrara et al., 1995).

The SAR technique is widely used in space, air, and ground platforms. In recent decades, Ground-Based Synthetic Aperture Radar (GBSAR) sensors have become more popular due to their capabilities to overcome some limitations of space and air sensors.

A GBSAR imaging system consists of a radar sensor moving on a mechanical rail. The resolution along the azimuth is directly related to the length of the mechanical rail. Thus, it can be said that the longer the length of the mechanical rail, the higher the resolution (Charvat, 2014).

Recently developed GBSAR systems operate on low power frequency modulated continuous wave (FMCW) signals, which can dramatically reduce the size and cost of the system. Another advantage of ground sensors is the high data collection rate (Pieraccini & Miccinesi, 2019). A typical GBSAR can image the surveyed area in an average time of one hour. The high acquisition rate makes it possible to monitor fast-moving targets. They also increase coherency between time series data and reduce processing errors such as phase ambiguity in Interferometric Synthetic Aperture Radar (InSAR) (Monserrat et al., 2014).

GBSAR monitoring can be applied to various fields of earth observation problems. Linear SAR (LISA) was the first GBSAR that was used for cultural heritage (Rudolf et al., 1999) and dam displacement (D. Tarchi et al., 1999) monitoring. Continuous monitoring of landslides was investigated by (Del Ventisette et al. (2011). Several other studies used GBSAR for monitoring civil structures (Huang et al., 2020), volcanic eruptions (Casagli et al., 2009), and glaciers (Akbari et al., 2018).

With the increasing applicability of GBSARs for remote sensing applications, new systems, and processing tools also have been developed in this area (Pieraccini & Miccinesi, 2019). Multiple input multiple outputs (MIMO) radars is a relatively new antenna configuration that can improve the radar's cross-range resolution with fewer antennas (Tarchi et al., 2012). Indeed, MIMO consists of N_{Rx} receiver antennas with Nyquist spacing and N_{Tx} transmitter antennas with non-Nyquist spacing. This geometry results in $N_{Rx} \times N_{Tx}$ virtual antennas. This condition increases the angular resolution by reducing the number of physical antennas. Moreover, MIMO antennas have better Doppler resolution than scanning arrays with longer lengths in the same period.

During the imaging period of the MIMO-SAR system, the signals can be transmitted by the transmitting antennas at the same or different times, and the receiving antennas can receive the echo signals at the same time. Thus, the orthogonality of the transmitted waves is one of the main conditions of the MIMO technique, which leads to having perpendicular received echoes. This condition is because orthogonality causes the received waves to be differentiated in the receivers and increases the ability to identify targets and increase the angular resolution compared to conventional radars (Tarchi et al., 2012).

In most recent studies, W band MIMO radars have found their way into remote sensing applications, especially for structural monitoring (Pieraccini & Miccinesi, 2019). These systems operate in the frequency range of 76-81 GHz and are mainly developed for automotive applications. However, the radar range equation shows that mmWave radars lead to weaker received power due to the shorter wavelength (Skolnik, 2008). Also, they are more sensitive to atmospheric layers than lower frequencies (Ulaby et al., 2014). These characteristics of mmWave radars make them suitable for short-range remote sensing applications using ground-based systems, while they are less useful in airborne or satellite systems. Recent studies by (Baumann-Ouyang et al., 2021) and (Ciattaglia et al., 2020) approve the applicability of these radars for structural monitoring with nearly micrometer accuracy. Moreover, few studies applied W band MIMO radars for monitoring real-world objects such as bridges (Baumann-Ouyang et al., 2022) and buildings (Gambi et al., 2019).

The angular discriminability of MIMO radars is limited to the number of generated virtual arrays. Currently available W band MIMO radars provide low angular resolution. In order to address this issue, one solution can be combining

mechanical rail with a MIMO radar. In our previous works, we investigated this solution with simulations, where we compared the results of MIMO-GBSAR with MIMO radar and monostatic GBSAR (Hosseiny et al., 2021a). In the current study, we aim to demonstrate the effectiveness of

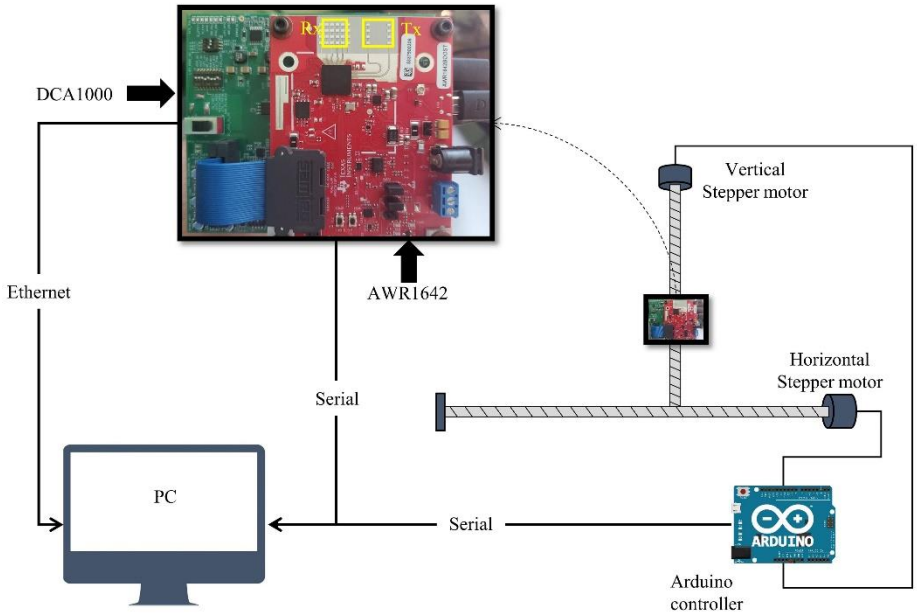

Figure 1. The schematic diagram of the sensor's movement on the rail

using a W-band MIMO radar combined with a mechanical rail to improve the cross-range resolution for target detection. Our developed system is based on a two-dimensional mechanical rail, and AWR1642BOOST from Texas Instruments (TI) is used as the MIMO radar. We show the results of various experiments and evaluate and discuss them from different aspects.

First, an overview of the utilized MIMO GBSAR system is provided in section 2. Section 3 provides the required theoretical background. The experimental results and discussions are presented in section 4. Finally, the concluding remarks are provided in section 5.

2. System Overview

In this study, we used AWR1642BOOST radar manufactured by Texas Instruments (TI). The radar generates a W-band FMCW signal. This sensor has two transmitting antennas and four receiving antennas, which leads to the creation of eight virtual arrays. The distance between the elements of the transmitter antenna is 2λ, i.e., 7.6 mm, and the distance between the elements of the receiver antenna is λ/2, i.e., 1.9 mm. The frequency of the transmitted waves can be between 76-81 GHz with a maximum bandwidth of 4 GHz. DCA100EVM capture card was used to transfer the captured signals from the radar to the computer. This card is connected to the sensor by a 60-pin cable, and raw information is transmitted to the computer through this card and Ethernet cable.

The sensor is installed on a mechanical rail 90 cm long horizontally and 50 cm in vertical directions. An Arduino microcontroller controls the movement and time duration of the mechanical rail. The sensor's movement of the rails is stopped after acquiring one pass of full signals. Then, after arranging the signals, the raw data cube is stored for further processing.

Figure 1 shows how the sensor moves on the rail. First, system parameters such as carrier frequency, bandwidth, chirp duration, and periodicity are configured and uploaded to the data acquisition system. After this step, the rail also starts to move in the horizontal direction. After the sensor reaches the end of the specified synthetic aperture length (e.g., 10 cm), the horizontal rail stops, and the vertical rail rises to the specified step size (e.g., 7.6 mm) along the vertical axis. Then, this time, it starts to move and collect data against the direction of the initial path in the horizontal direction until it reaches the starting point. This procedure repeats till the end of the scanning process.

3. Theoretical Background

GBSAR image consists of a complex number for each image pixel with the In-phase and Quadrature (I and Q) components of the received echoes. The signal phase and amplitude can be derived from this complex number (Monserrat et al., 2014). The amplitude can be used to interpret the image scene, and the phase information is used for measuring the range and deformation (Ulaby et al., 2014). The image dimensions are the range and cross-range directions.

The range resolution can be obtained through an FMCW de-ramping rang compression process and is inversely proportional to the bandwidth according to Eq. (1):

$$\Delta R = \frac{C}{2B} \tag{1}$$

where ΔR is the range resolution, C is the speed of light and B is the bandwidth of the transmitted signal (Lacomme, Marchais, Hardange, & Normant, 2001). On the other hand, the resolution along the cross-range direction is achieved through advanced MIMO SAR processing (Tarchi et al., 2012). The theoretical cross-range resolution is provided in Eq. (2):

$$\rho_{cr} = \frac{\lambda R}{2l} \tag{2}$$

where ρ_{cr} is the cross-range resolution, R is the slant range and l is the effective length of the antenna in the direction where beam width is to be measured. As can be seen, the resolution along the cross-range depends on the length of the antenna. Since the length of the antenna is small in the MIMO-Radar mode, the resolution in the cross-range direction is low. For this reason, the sensor is installed on a mechanical rail in order to improve the cross-range resolution. So it can be said that the main idea of SAR is to increase the resolution of the radar in the cross-range direction by collecting data from different cross-range positions of the radar (Hosseiny et al., 2021).

It is necessary to use signal compression on the range and cross-range dimensions to finally generate a focused image (Demirci et al., 2011). The process of storing and processing the signal received by the MIMO-SAR sensor is shown in Figure 2.

The radar sensor continuously and with a constant velocity moves along the horizontal aperture. The radar's movement along the vertical axis is step-wise, which means that at each vertical step, radar starts its continuous pass in the horizontal axis, and then this procedure repeats for each vertical step till the end of the scanning process. Accordingly, we used MIMO virtual arrays along vertical directions due to the radar's step-wise movement. MIMO processing gives us bigger sampling steps than conventional monostatic GBSARs (Zhou et al., 2020).

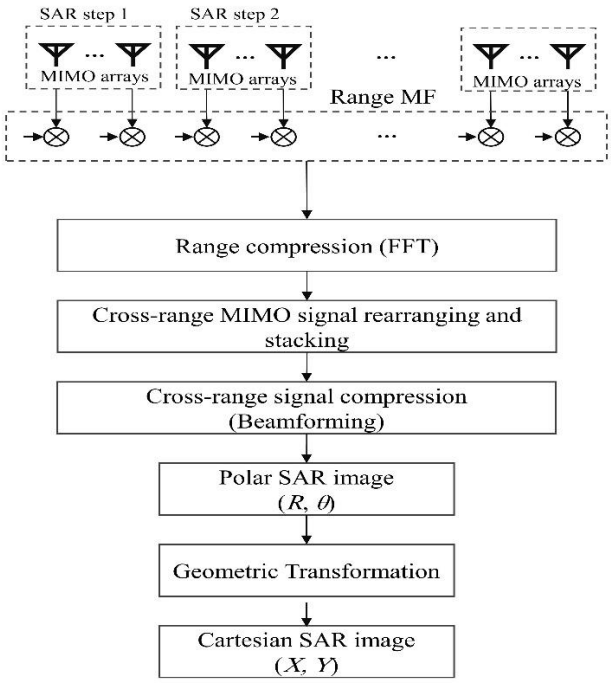

Figure 2. MIMO GBSAR processing chain

More specifically, the required sample size to avoid spectrum fold and aliasing are $\lambda/4$, while with MIMO processing and generating bigger virtual arrays we can increase SAR sampling size to $N_v\lambda/4$, where $N_v=N_{Tx}\times N_{Rx}$ is the number of virtual arrays (Hosseiny et al., 2021b). For instance, AWR1642 with 3.9 mm wavelength, two Tx antennas, and four Rx antennas can generate eight virtual arrays after MIMO processing. Subsequently, we can consider around 7.6 millimeter sampling size in cross-range direction. Thus, for a 3D SAR imaging scenario, the acquired raw signals are stored in a four-dimensional $N_r\times N_{az}\times N_{el}\times N_v$ matrix, where N_r, N_{az}, and N_{el} are the number of samples in range, azimuth, and elevation directions. Raw data is acquired by the MIMO GBSAR system. For further processing, it is required to reshape the obtained matrix to a three-dimensional matrix, where the MIMO virtual arrays are rearranged in their acquisition direction. For instance, if the MIMO arrays are in an elevation direction, the reshaped 3D raw data-cube size would be $N_r\times N_{az}\times(N_{el}\times N_v)$. The obtained data cube is the same size as the obtained data by monostatic SAR, but with N_v times fewer repeat passes in the elevation direction, which results in a faster data acquisition process. Thus, obtaining SAR focused image by MIMO-GBSAR can be summarized as the following steps (see processing flow in Figure 2):

1- Transmit and receive signals through MIMO radar at each step on the GBSAR rail
2- Dechirping process of the received signal via matched filtering
3- Signal compression in range direction (range FFT)

4- Rearranging and stacking the received signals from MIMO virtual arrays
5- Signal compression in cross-range directions (horizontal or vertical axes)
6- Geometrical transformation from Polar coordinate system to Cartesian system

As shown in Figure 1 from the previous section, at this stage, by moving the sensor along the horizontal axis, the sensor produces and sends signals, and the receiver antennas receive the echo signals and finally store them in the form of a data cube by virtual arrays. The transmitted chirp signal is provided in Eq. (3).

$$S_t = \exp(j\,2\pi f_c t + j\,\pi c_r t^2) \quad (3)$$

In this equation, S_t is the transmitted signal, f_c is the carrier frequency and C_r is the chirp rate of the signal. As mentioned in the introduction, the orthogonality of the transmitted signals is the main condition of MIMO sensors, which causes differences in the received signals. Eq. (4) expresses the law of orthogonality between two independent signals, where their correlation must be zero.

$$\int_0^T S_m(t) S_k^*(t) dt = 0 \quad (4)$$

In this equation, S_m and S_k^* are two different transmitted signals that are limited between 0 and T, and * is the Conjugate symbol (Tarchi et al., 2012).

The received signal is actually the same as the transmitted signal with a time delay as shown in Eq. (5).

$$S_r = \exp(j\,2\pi f_c (t - t_d) + j\,\pi C_r (t - t_d)^2) \quad (5)$$

In this equation, S_r is the received signal, In this equation, S_r is the received signal, t_d is the time delay. To identify the targets, the received signal must be compressed. Signal compression is done by the dechirping process, which is similar to the matched filter (Carrara et al., 1995). Therefore, the received and transmitted signals are convolved in the mixer and the Intermediate Frequency (IF) signal is created in the form of Eq. (6).

$$S_b = \exp(j\,2\pi(C_r t_d t + f_c t_d - \frac{1}{2} C_r t_d^2)) \quad (6)$$

where Sb is called IF or beat signal. By doing this processing at this stage, the carrier frequency is removed from the signal. To complete the range compression process, Fourier transform (FT) is applied to the dechirped signal, which creates the range compressed signal. This processing results in obtaining phase and frequency information of the IF signal, which finally leads to the calculation of the distance between the sensor and the target (Li et al., 2015).

In the next step, signals in cross-range directions are rearranged and stacked. This step's objective is to synthesize a large effective antenna aperture—with a correspondingly narrow beam width and high angular resolution—using a distributed network of much smaller physical antennas (Ulaby et al., 2014).

Now, to identify the targets in the azimuth direction, it is necessary to apply cross-range compression. For this reason, the Fourier transform is once again applied.

The SAR image is in the polar coordinate system where one axis is along the range and the other axis is along the azimuth angle. For this reason, it is necessary to convert the coordinates from the polar coordinate system to the Cartesian coordinate system using the following transformation shown in Eq. (7).

$$\begin{cases} X = R.\sin\theta \\ Y = R.\cos\theta \end{cases} \quad (7)$$

where (X,Y) is the Cartesian coordinate of a point target located at (R,θ) in the Polar coordinate system.

4. Experiments and Results

This section describes and discusses the results obtained from the experiments based on the developed GBSAR system. The system's parameters are shown in Table 1, where the radar sensor's operating frequency spans from 76-81 GHz with a maximum bandwidth of 4 GHz. Vertical and horizontal mechanical rails make it feasible to increase the length of the synthetic aperture up to 50 cm and 90 cm in vertical and horizontal directions, respectively. We occupied the whole 4 GHz signal bandwidth in order to obtain the maximum range resolution, which is about 4 cm. Hence, having 512 range samples for each of the recorded digital signals, the maximum operating range of our system would be about 20 meters. More details about the relations between the signal bandwidth and the maximum range of our radar system can be found in our previous work (Hosseiny et al., 2021b).

In order to evaluate the effectiveness of the GBSAR, we operated experiments in a controlled scenario. During these experiments, the cross-range resolution, and focusing capabilities of the obtained images were compared between the SAR configuration, conventional uniform linear array (ULA), and MIMO radar configurations.

Figure 3 shows the study area and the GBSAR system setup. Two 10 cm trihedral corner reflectors were located in front of the radar. One is located nearer to the radar and the other one has a greater slant range with different cross-range angles.

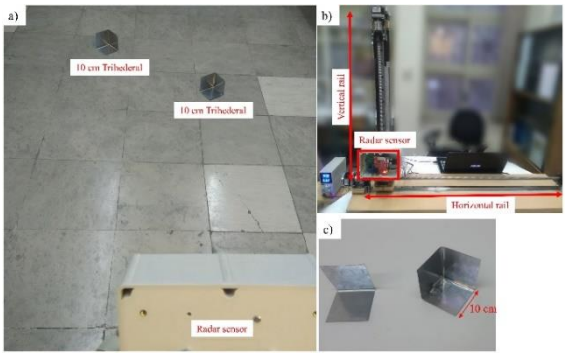

Figure 3. System setup: a) Imaging scene. b) GBSAR prototype. c) Used corner reflectors as targets.

Table 1. GBSAR parameters

Parameter	Value
Radar model	TI-AWR1642BOOST
Signal type	Linear FMCW
operating frequency (f_c)	76-81 GHz
Wavelength (λ)	0.0039 m
Bandwidth (B)	4 GHz
Range samples	512
Sweep time (τ)	60 µs
Peak power (P)	1.5 mW
Number of transmitters (N_{Tx})	2
Number of receivers (N_{Rx})	4
Horizontal rail length (L_h)	0.9 m
Vertical rail length (L_v)	0.5 m
Tx Gain (G_{Tx})	30 dB
Rx Gain (G_{Rx})	30 dB

According to our previous work (Hosseiny et al., 2022), we showed that based on the presence of a target in radar's near-field region ($R_t<L^2/\lambda$, where R_t is the target's distance to the radar, and L is the aperture length) increasing the aperture length can degrade the cross-range resolution in Fourier focusing algorithm hyperbolically. Thus, in this study, we only used a 10 cm synthetic aperture, in order to avoid the defocusing effects of long synthetic aperture length in near-field targets, due to the non-ideal imaging geometry. The focused image can be obtained by compressing the raw signal array in range and cross-range directions. Figure shows the studied scene's focused images, including the corner reflectors in the four different radar imaging configurations. As can be seen from these images, in the case of using ULA and MIMO radar, targets appeared dispersed in the focused image and wide in the cross-range axis. More specifically, both targets' cross-range locations seem to be very close according to the ULA's radar image (Figure -a), while in the case of MIMO radar (Figure -b), targets' cross-range signals seem to be focused with better resolution, hence the cross-range focusing looks more accurate. Compared to these configurations, targets in SAR imaging scenarios Figure -c, d) appeared to be more focused and the obtained images seem to have a higher signal-to-clutter ratio (SCR).

For a detailed view, Figure depicts the normalized point spread function (PSF) of the farther target in terms of cross-range direction for the investigated imaging configurations. It can be seen that the ULA configuration, with only using

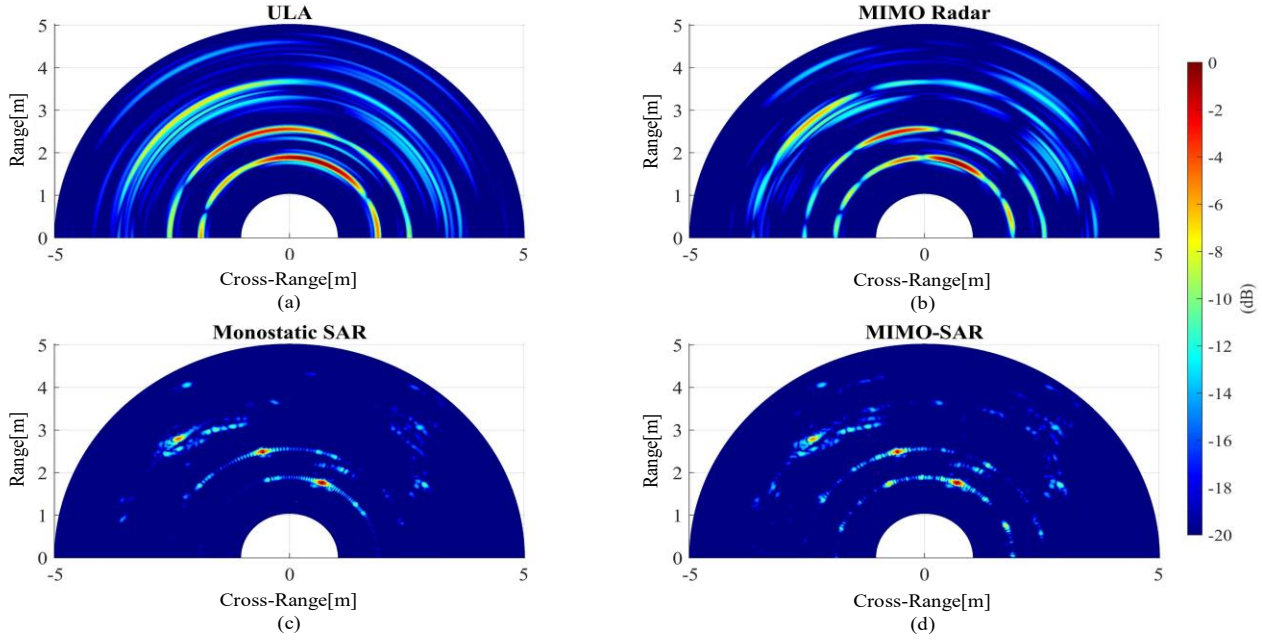

Figure 4. SLC images of study area: (a) based on four ULAs to form synthetic aperture in cross-range direction. (b) based on eight MIMO virtual arrays in MIMO radar configuration. (c) based on conventional monostatic SAR configuration. (d) based on MIMO SAR configuration.

one transmitter and four receiver antennas, provides a wide cross-range signal pattern of the target. MIMO configuration could improve the ULA's results by adding an extra transmitter and providing eight virtual antennas, which is twice the ULA configuration. It can be seen that the focused target by SAR configurations signal shows narrower width, while the background noise level is much lower than in ULA and MIMO radar cases. It is also noticeable that MIMO SAR obtained a similar PSF to monostatic SAR while requiring fewer sampling steps.

Table 2. Quantifying the cross-range focusing capability of MIMO SAR configuration compared to the ULA and MIMO radar configurations

	ULA	MIMO Radar	Monostatic SAR	MIMO SAR
Along track steps*	-	-	104	13
Synthetic aperture length (mm)	7.6	15.2	99	99
3dB Angular resolution (rad)	0.489	0.262	0.014	0.014
PSLR (dB)	10	13.8	21.45	21.45
SCR (dB)	9.34	11.97	25.02	22.98

* required along track steps to generate a 10 cm synthetic aperture

Table 2 quantifies the focusing capability of the investigated radar imaging configurations based on three metrics of 3 dB angular resolution, peak sidelobe ratio (PSLR), and SCR. The mentioned metrics were evaluated on the signals of the two CRs in the obtained images and their average values were reported in this paper. Accordingly, without using MIMO capability, the conventional ULA can synthesize a 3.8 mm length antenna, with 0.49 rad cross-range discriminability, while in MIMO configuration the length of the synthesized antenna is twice. Accordingly, the obtained cross-range resolution based on our experiments is 0.26 radian. In comparison, in GBSAR configuration, we increased the aperture length to 99 mm, which improved the angular discriminability up to 0.014 radians. Moreover, MIMO SAR image obtained 21.45 dB and 22.98 dB for PSLR and SCR metrics, respectively. This means that in our case study SAR configuration was able to increase the signal level and suppress the background clutters more than 10 dB. More specifically, Figure shows

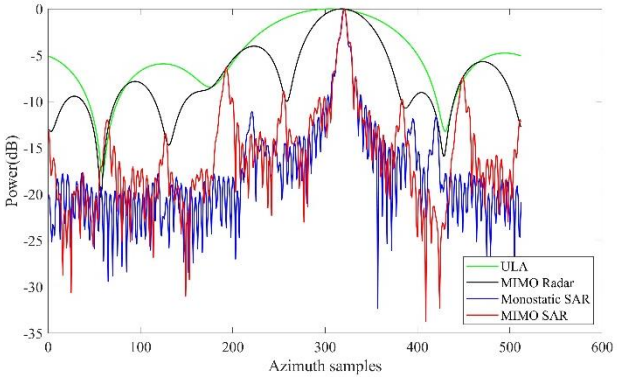

Figure 5. Cross-range signal compression capability of MIMO SAR signal compared to the conventional four ULAs and eight virtual arrays of MIMO radar signal

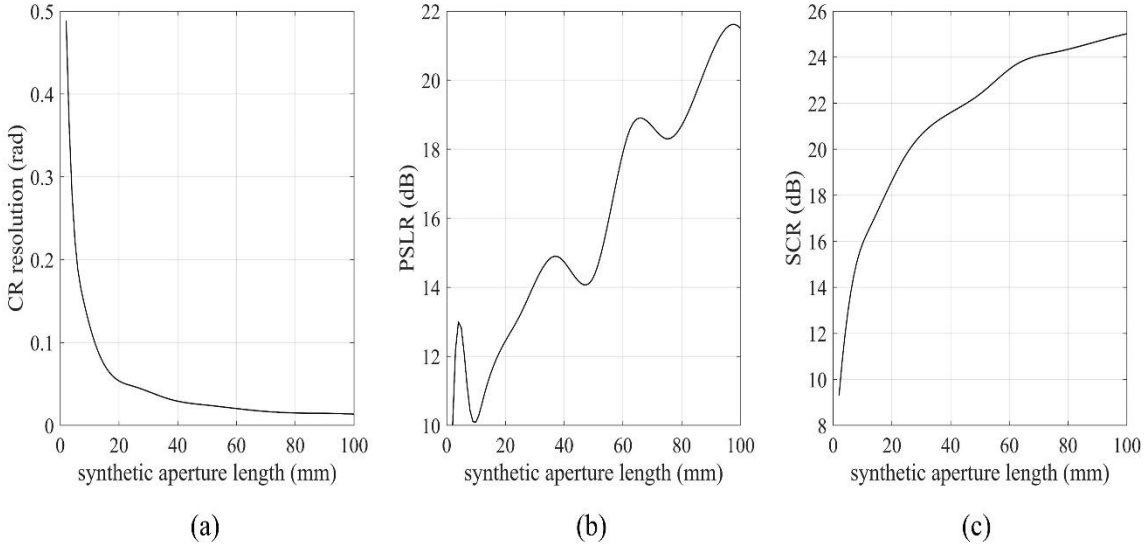

Figure 6. Relation between the synthetic aperture length and (a) cross-range resolution. (b) PSLR. (c) SCR

the relation between the synthetic aperture length and the mentioned radar image quality metrics.

4. 1. MIMO GBSAR vs Monostatic GBSAR

This subsection aims to demonstrate a deeper comparison between the obtained MIMO-GBSAR and Monostatic-GBSAR images. According to Figure -c, d, both configurations show similar target focusing capabilities. Both configurations obtained the same cross-range resolution. However, MIMO GBSAR could achieve this resolution with only 13 data acquisitions for a 10 cm synthetic aperture length in the cross-range direction. Comparing the focusing quality, both MIMO and monostatic GBSAR images provided equal PSLR values. However, monostatic GBSAR obtained higher SCR value (25.02 dB) compared to the MIMO GBSAR image (22.98 dB) (see Table 2)

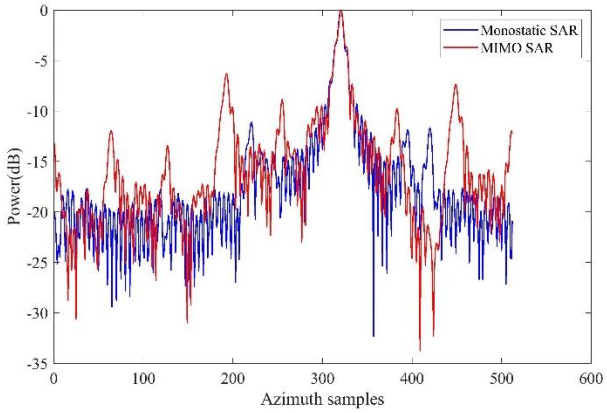

Figure 7. Cross-range signal profile of a corner reflector in MIMO GBSAR and monostatic GBSAR configurations

Figure 7 compares the focused signals of MIMO GBSAR and monostatic GBSAR in cross-range direction. Although it can be observed that both configurations provided similar peak signals in target's location, we can notice the higher power of unwanted artefacts in the MIMO GBSAR signal. **Error! Reference source not found.** shows the unwrapped phase tracks of MIMO GBSAR and monostatic GBSAR configurations in cross-range direction. It can be noticed that monostatic GBSAR provides more phase stability. The lower performance of MIMO GBSAR could be due to signal interferences between virtual arrays, which can be due to their coarse cross-range resolution and internal noises. In our future studies, we aim to address this issue and propose a practical solution.

4. 2. Investigating the effects of rail fluctuations

One main problem of using GBSAR can be the signal errors caused by the sensor's fluctuations during its travel on the mechanical rail. In order to analyze this issue, we extracted one of the corner reflector's phase histories when the radar sensor travels 90 cm in a cross-range direction (Figure 9). Comparing the zoomed areas in the phase history of the target, it is noticeable that the sensor's fluctuations in the starting steps of the rail (Figure 9c, 9d) are stronger than the rest of it (Figure 9c, 9d). Figure compares the focused cross-range signal in two portions of the SAR signal in cross-range direction: the first portion is the first 200 azimuth samples, where the sensor's fluctuations are severe and the second focused signal was obtained from the next azimuth samples, where the sensor has lower fluctuations. According to the evaluations provided in Table 3 strong sensor fluctuation caused to more than 5 dB decrease in the focused signal's PSLR and SCR.

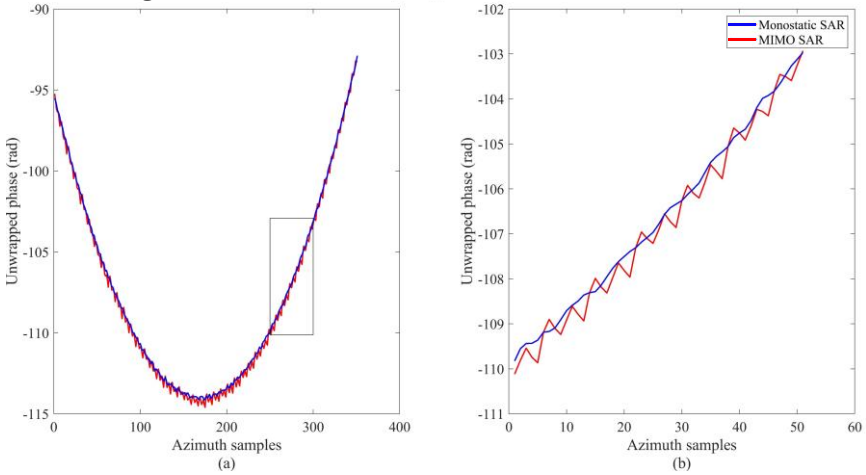

Figure 8. (a) Unwrapped cross-range phase track of corner reflector in MIMO GBSAR and monostatic GBSAR configurations. (b) zoomed area

Therefore, in order to overcome this issue, we ignore the signals that came from the sensor's first steps on the GBSAR's rail.

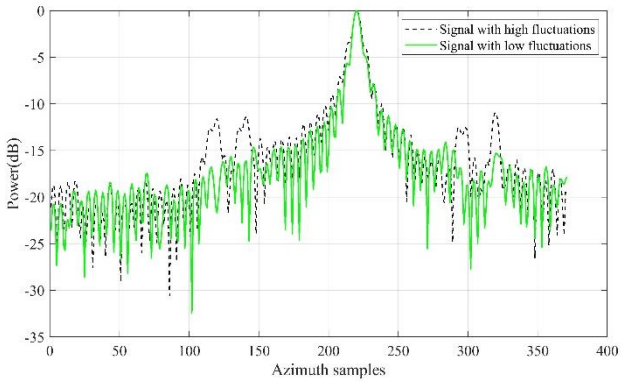

Figure 10. Obtained PSF signals in the presence of strong and weak sensor fluctuations

Table 3. Evaluating the effect of the sensor's fluctuations on the focused cross-range signal

Scenario	PSLR (dB)	SCR (dB)
High fluctuations	12.86	20.19
Low fluctuations	17.63	25.50

5. conclusion

MIMO radars have emerged in remote sensing and earth observation applications in the past few years. More specifically, mmWave MIMO offers a lightweight and cost-efficient radar sensor with angular discrimination capability. However, MIMO radars provide a limited angular resolution, which may not suffice in earth observation applications. This study demonstrated the effectiveness of mechanical rail and MIMO radars in improving the radar angular or cross-range resolution. To this end, a MIMO GBSAR prototype was developed. The presented system contains two mechanical rails in horizontal and vertical directions, where the radar sensor can move along them. TI's AWR1642BOOST MIMO radar with eight virtual arrays was used as the core radar sensor. The MIMO GBSAR was evaluated in a controlled scenario, where the SLC image of metallic trihedral corner reflectors was generated from the collected signals. According to the results, the developed MIMO GBSAR improved more than 10 dB in the PSLR and SCR values compared to the ULA and MIMO radar configurations and improved the angular resolution to 0.014 radians. The results were very close to the conventional monostatic GBSAR with similar angular resolution and PSLR but with slightly weaker SCR. This validates the developed system's capability while providing a faster image acquisition process than conventional GBSAR. Moreover, the effect of the rail's mechanical fluctuations on the obtained SAR image was investigated. The results showed SCR reduction when high fluctuations were present, which mainly happened at the starting steps of data acquisition. At this point, we remove and ignore the radar sample obtained during the rail's first steps to overcome this issue. Our future works will be focused on the interferometric capabilities of the mmWave MIMO GBSAR for displacement and moving target monitoring.

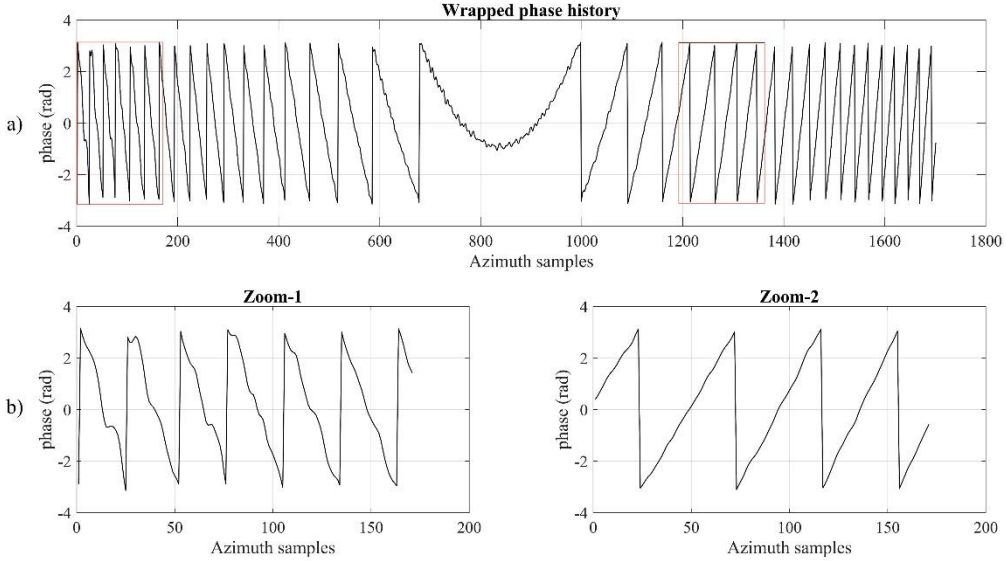

Figure 9. Phase history of the corner reflector presented in the imaging scene (a) during the formation of 90 cm synthetic aperture (b) zoomed areas

References

Akbari, V., Lauknes, T. R., Rouyet, L., Negrel, J., & Eltoft, T. (2018, 22-27 July 2018). Validation of sar iceberg detection with ground-based radar and gps measurements. IGARSS 2018 - 2018 IEEE International Geoscience and Remote Sensing Symposium.

Ao, D., & Datcu, M. (2018). Ship azimuth velocity estimation in TerraSAR-X data based on minimum-entropy criterion. Proceedings of the European Conference on Synthetic Aperture Radar, EUSAR (Vol. 2018-June).

Artese, S., & Nico, G. (2020). TLS and GB-RAR measurements of vibration frequencies and oscillation amplitudes of tall structures: an application to wind towers. Applied Sciences 2020, Vol. 10, Page 2237, 10(7), 2237. https://doi.org/10.3390/APP10072237

Bamler, R., & Hartl, P. (1998). Synthetic aperture radar interferometry. Inverse Problems, 14(4), R1.

Baumann-Ouyang, A., Butt, J.A., Wieser, A. (2022). Bridge deformations during train passage: monitoring multiple profiles using concurrently operating MIMO-SAR sensors. In 5th Joint International Symposium on Deformation Monitoring (JISDM). Valencia, Spain.

Baumann-Ouyang, A., Butt, J. A., Salido-Monzú, D., & Wieser, A. (2021). MIMO-SAR interferometric measurements for structural monitoring: accuracy and limitations. Remote Sensing 2021, Vol. 13, Page 4290, 13(21), 4290. https://doi.org/10.3390/RS13214290

Carrara, W. G., Goodman, R. S., & Majewski, R. M. (1995). Spotlight synthetic aperture radar : signal processing algorithms. Boston : Artech House. Retrieved from https://searchworks.stanford.edu/view/3116166

Casagli, N., Tibaldi, A., Merri, A., Del Ventisette, C., Apuani, T., Guerri, L., … Tarchi, D. (2009). Deformation of Stromboli Volcano (Italy) during the 2007 eruption revealed by radar interferometry, numerical modelling and structural geological field data. Journal of Volcanology and Geothermal Research, 182(3–4), 182–200.

Charvat, G. L. (2014). Small and short-range radar systems. CRC Press.

Ciattaglia, G., De Santis, A., Disha, D., Spinsante, S., Castellini, P., & Gambi, E. (2020). Performance evaluation of vibrational measurements through mmwave automotive radars. Remote Sensing 2021, Vol. 13, Page 98, 13(1), 98. https://doi.org/10.3390/RS13010098

Del Ventisette, C., Intrieri, E., Luzi, G., Casagli, N., Fanti, R., Leva, D., Keefer, D. (2011). Using ground based radar interferometry during emergency: the case of the A3 motorway (Calabria Region, Italy) threatened by a landslide. Natural Hazards & Earth System Sciences, 11(9).

Demirci, Ş., Yigit, E., & Ozdemir, C. (2011). A comparison of focusing algorithms for ground based SAR system.

Farina, P. (2011). IBIS-M, an innovative radar for monitoring slopes in open-pit mines.

Gambi, E., Ciattaglia, G., & De Santis, A. (2019). Automotive radar application for structural health monitoring. wit Transactions on The Built Environment, 189, 79–89.

Hosseiny, B., Amini, J., Esmaeilzadeh, M., & Nekoee, M. (2021). Evaluating an S-band ground-based synthetic aperture radar imaging system for LFMCW SAR processing. Earth Observation and Geomatics Engineering, 5(3). https://doi.org/10.22059/EOGE.2021.306032.1084

Hosseiny, B., Amini, J., & Safavi-Naeini, S. (2021a). Evaluating the deformation monitoring capability of a ground based SAR system with MIMO antenna. Engineering Journal of Geospatial Information Technology, 9(1), 21–40. Retrieved from http://jgit.kntu.ac.ir/article-1-815-en.html

Hosseiny, B., Amini, J., & Safavi-Naeini, S. (2021b). simulation and evaluation of an mm-Wave MIMO ground-based SAR imaging system for displacement monitoring. In 2021 IEEE International Geoscience and Remote Sensing Symposium IGARSS (pp. 8213–8216). IEEE. https://doi.org/10.1109/IGARSS47720.2021.9553347

Hosseiny, B., Amini, J., & Safavi-Naeini, S. (2022). Comparison study of signal processing algorithms for 3d sar imaging of mm-wave gbsar system. Engineering Journal of Geospatial Information Technology, 10(1), 69–87. Retrieved from http://jgit.kntu.ac.ir/article-1-857-en.html

Huang, Q., Wang, Y., Luzi, G., Crosetto, M., Monserrat, O., Jiang, J., … Ding, Y. (2020). Ground-based radar interferometry for monitoring the dynamic performance of a multitrack steel truss high-speed railway bridge. Remote Sensing 2020, Vol. 12, Page 2594, 12(16), 2594. https://doi.org/10.3390/RS12162594

Intrieri, E., Di Traglia, F., Del Ventisette, C., Gigli, G., Mugnai, F., Luzi, G., & Casagli, N. (2013). Flank instability of Stromboli volcano (Aeolian Islands, Southern Italy): Integration of GB-InSAR and geomorphological observations. Geomorphology, 201, 60–69. https://doi.org/https://doi.org/10.1016/j.geomorph.2013.06.007

Lacomme, P., Marchais, J.-C., Hardange, J.-P., & Normant, E. (2001). Air and spaceborne radar systems: An introduction (Vol. 108). William Andrew.

Li, C., Chen, W., Liu, G., Yan, R., Xu, H., & Qi, Y. (2015). A noncontact FMCW radar sensor for displacement measurement in structural health monitoring. Sensors, 15(4), 7412–7433.

Luzi, G., Pieraccini, M., Mecatti, D., Noferini, L., Macaluso, G., Galgaro, A., & Atzeni, C. (2006). Advances in ground-based microwave interferometry for landslide survey: a case study. International Journal of Remote

Sensing, 27(12), 2331–2350. https://doi.org/10.1080/01431160600554975

Luzi, G., Crosetto, M., & Monserrat, O. (2010). Advanced Techniques for Dam Monitoring.

Luzi, G., Pieraccini, M., Mecatti, D., Noferini, L., Macaluso, G., Tamburini, A., & Atzeni, C. (2007). Monitoring of an alpine glacier by means of ground-based SAR interferometry. IEEE Geoscience and Remote Sensing Letters, 4(3), 495–499.

Martinez-Vazquez, A., & Fortuny-Guasch, J. (2008). A GB-SAR processor for snow avalanche identification. IEEE Transactions on Geoscience and Remote Sensing, 46(11), 3948–3956. https://doi.org/10.1109/TGRS.2008.2001387

Miccinesi, L., Consumi, T., Beni, A., & Pieraccini, M. (2021). W-band MIMO GB-SAR for bridge testing/monitoring. Electronics, 10(18), 2261.

Monserrat, O., Crosetto, M., & Luzi, G. (2014). A review of ground-based SAR interferometry for deformation measurement. ISPRS Journal of Photogrammetry and Remote Sensing, 93, 40–48.

Pieraccini, M., & Miccinesi, L. (2019). Ground-based radar interferometry: A bibliographic review. Remote Sensing, 11(9), 1029.

Richards, M. A., Scheer, J., Holm, W. A., & Melvin, W. L. (2010). Principles of modern radar. Citeseer.

Skolnik, M. I. (2008). Radar handbook. McGraw-Hill Educatio

Rudolf, H., Leva, D., Tarchi, D., & Sieber, A. J. (1999). Mobile and versatile SAR system. In International Geoscience and Remote Sensing Symposium (IGARSS) (Vol. 1, pp. 592–594). IEEE. https://doi.org/10.1109/igarss.1999.773575

Tarchi, D., Rudolf, H., Luzi, G., Chiarantini, L., Coppo, P., & Sieber, A. J. (1999). SAR interferometry for structural changes detection: a demonstration test on a dam. In International Geoscience and Remote Sensing Symposium (IGARSS) (Vol. 3, pp. 1522–1524). IEEE. https://doi.org/10.1109/igarss.1999.772006

Tarchi, D., Antonello, G., Casagli, N., Farina, P., Fortuny-Guasch, J., Guerri, L., & Leva, D. (2005). On the use of ground-based SAR interferometry for slope failure early warning: the cortenova rock slide (Italy). In K. Sassa, H. Fukuoka, F. Wang, & G. Wang (Eds.), Landslides: Risk Analysis and Sustainable Disaster Management (pp. 337–342). Berlin, Heidelberg: Springer Berlin Heidelberg. https://doi.org/10.1007/3-540-28680-2_43

Tarchi, D., Oliveri, F., & Sammartino, P. F. (2012). MIMO radar and ground-based SAR imaging systems: Equivalent approaches for remote sensing. IEEE Transactions on Geoscience and Remote Sensing, 51(1), 425–435.

Ulaby, F., Long, D., Blackwell, W., Elachi, C., Fung, A., Ruf, C., … Van Zyl, J. (2014). Microwave radar and radiometric remote sensing. Ann Arbor: University of Michigan Press. Retrieved from http://titlealert.alkemlibrary.com/attachments/546/Artech House ABI - Mar 15 - Ulaby.pdf

Weihing, D., Hinz, S., Meyer, F., Laika, A., & Bamler, R. (2006). Detection of along-track ground moving targets in high resolution spaceborn SAR images.

Zhou, Y., Wang, W., Chen, Z., Wang, P., Zhang, H., Qiu, J., … Wang, R. (2020). Digital beamforming synthetic aperture radar (DBSAR): Experiments and performance analysis in support of 16-channel airborne x-band sar data. IEEE Transactions on Geoscience and Remote Sensing, 1–15. https://doi.org/10.1109/tgrs.2020.3027691